Front. Optoelectron. 2016, 9(2): 290–300
DOI 10.1007/s12200-016-0610-7

RESEARCH ARTICLE

Integrated coherent combining of angled-grating broad-area lasers

Yunsong ZHAO (✉)[1,2], Yeyu ZHU[1,2], Lin ZHU[1,2]

1 Electrical and Computer Engineering Department, Clemson University, Clemson SC 29634, USA
2 Center for Optical Material Science and Engineering Technologies, Clemson University, Clemson SC 29634, USA

Abstract In this paper, we investigated coherent beam combining of angled-grating broad-area lasers in a completely integrated approach. We obtained the simultaneous coherent beam combining and single transverse mode operation on a single chip through the integrated coupling regions and the transverse Bragg resonance (TBR) gratings, respectively. The proposed combining method can be easily extended to a zigzag-like laser array. We analyzed the scalability of the zigzag-like combining structure and compared it with other coherent combining methods. Two and six angled-grating broad-area lasers are fabricated and coherently combined by use of the proposed method. The high contrast interference fringes within an overall single lobe envelope in the measured far field prove that the emitters in the array are indeed coherently combined. By p-side-down bonding, we obtained over 1 W output power with over 90% combining efficiency in the two coherently combined lasers.

Keywords semiconductor lasers, angled-grating broad-area lasers, coherent beam combining, high power, high brightness

1 Introduction

A large emitting aperture is needed for high power operation of semiconductor lasers, since it can reduce the power density on the facet to overcome the catastrophe optical damage (COD) [1,2] and help with the heat dissipation. For high brightness, single transverse mode is required to obtain a diffraction-limited, single lobe far field. However, commonly used broad-area edge-emitting semiconductor lasers cannot satisfy these requirements simultaneously, because the weak modal control based on index guiding is not robust against the index perturbation induced by current injection and nonlinear effects. The angled-grating broad-area laser [3 – 5] was proposed to accomplish both requirements, i.e., high brightness operation with a broad emitting aperture. In this design, the transverse Bragg resonance (TBR) grating is used to confine Bragg modes with large modal discrimination. And the angled cavity favors the Bragg mode as the single waveguide mode by filtering out other spatial modes. This design has already been proved to deliver over 1 W output power per emitter with near-diffraction-limited beam quality.

In order to obtain even higher output power, beam combining techniques can be used. There are two methods of beam combining: one is coherent beam combining and the other one is incoherent (wavelength) beam combining [6 – 8]. The main difference between these two approaches is that there is constant phase difference between emitters in a coherently combined laser array while in an incoherently combined laser array, the phase difference is random and usually each emitter has a different wavelength. The incoherent beam combining does not improve the brightness, since the divergence angle of the combined beam is more or less the same as that of a single emitter. The ideal coherent beam combining of N single emitters with the filling factor around one can improve the brightness by N times because the divergence angle of the combined beam becomes $1/N$ of that of a single emitter [6,9,10].

Depending on whether external components are needed, coherently combined laser arrays can be divided into two categories. The first category can be monolithically implemented. Several examples are evanescently coupled laser arrays [11,12] chirped and Y-coupled laser arrays [13 – 15] and leaky wave coupled (anti-guided) laser arrays [16,17]. These structures are only compatible with narrow stripe index-guided single-mode lasers or gain-guided

Received January 27, 2016; accepted February 12, 2016

E-mail: yunsonz@g.clemson.edu

lasers. Thus, the total width of conventional coherent diode laser arrays is limited less than a few hundred microns. The second category requires external cavities or phase control, including externally injection-locked laser arrays [18,19], Talbot cavity laser arrays [20–22], self-Fourier cavity laser arrays [23,24] and master oscillator power amplifier (MOPA) arrays [25–32]. Since external cavities and/or accurate phase control are needed, these systems in the second category are usually complex, bulky and not robust [6,33]. Therefore, there has not been an integrated solution for coherent combining of broad-area lasers.

In this paper, we demonstrate monolithic coherent beam combining of angled-grating broad-area diode lasers. The angled-grating broad-area laser is used as the building element. We use Bragg diffraction to directly couple two angled-grating broad-area lasers by overlapping their output facets. The overlapped region forms a triangular photonic crystal coupler that coherently combines the two lasers. Multiple angled-grating broad-area lasers can be coherently combined by simply extending this design into a zigzag-like coherently coupled laser array. We also analyze the scalability of the zigzag-like laser array and compare it with other common passive coherent beam combining structures. We fabricate and characterize a coupled laser of two emitters and a laser mini bar of six emitters. The measured near field and far field profiles prove that out approach can obtain coherent beam combining and near-diffraction-limited beam quality at the same time for broad-area diode lasers.

2 Simultaneous single mode control and coherent beam combining through Bragg diffraction

Figure 1 shows a schematic of the two coherently combined angled-grating lasers. The combined laser cavity consists of two sets of angled-gratings that tilt to the opposite directions with the same angle. The overlap area of the two gratings defines a two dimensional coupling region. The phase locking of two emitters is obtained by the wave coupling through Bragg diffraction in this overlap region.

The calculated mode of the single angled-grating broad-area laser is a snake-like zigzag mode which consists of two planewave-like components in resonance with the grating, R_1 and R_2, as shown in Fig. 2(a). The angles between R_1/R_2 and the grating direction are both equal to θ, the grating tilted angle. The wavevectors of R_1, R_2 and the grating satisfy the resonance condition: $\boldsymbol{k}_{R_1} + \boldsymbol{k}_G = \boldsymbol{k}_{R_2}$, as shown in the inset of Fig. 2(a). The propagation direction of the R_1 component is perpendicular to the facet and that of R_2 is tilted. When R_1 is reflected by the facet, it will be fed back to the cavity; but for R_2, it will be lost. Therefore, once used as the laser cavity, the angled-grating resonator

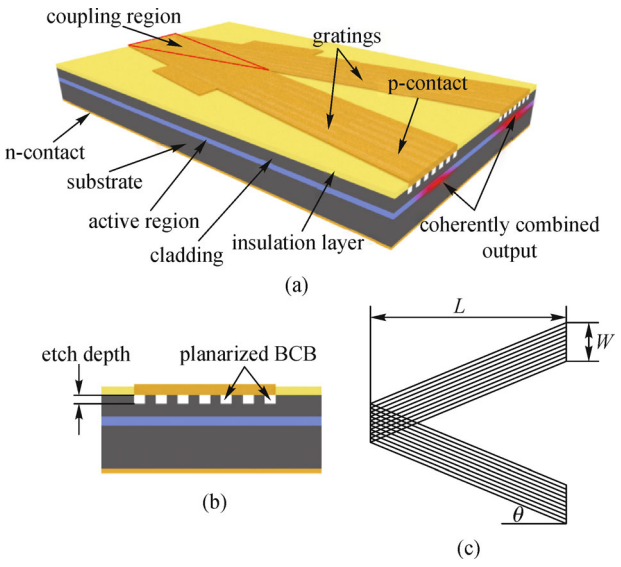

Fig. 1 Schematic of a coherently combined angled-grating laser. (a) Planar geometry of the combined angled-grating laser. Two coherently combined emitters (the output from two legs in the coupled structure) constructively interfere in the far field; (b) cross-section structure of a single emitter; (c) L and W are the length and width of a single emitter, respectively. θ is the tilt angle of the grating

will self-adaptively select the cavity mode with the maximum R_1 and the minimum R_2 component at the facets. This mode profile is shown in Fig. 2(b) which is simulated by finite-different time-domain (FDTD) method. Through the large modal discrimination provided by the grating and strong spatial filtering provided by the angle geometry, angled-grating broad-area (>100 μm) diode lasers can obtain stable single mode operation at high current injection level [3,4,34].

Coherent combining of two symmetrical angled-grating emitters that tilt to the opposite directions is obtained by overlapping them with each other at one facet, as shown in Fig. 2(c). The overlapped region forms a triangular 2D periodic structure (photonic crystal), which enables the cross coupling of two single emitters through Bragg diffraction. Outside the coupling region, the cavity modes are the same as that in a single angled-grating emitter. For simplicity, we only take into consideration of the first order Bragg diffraction in the coupling region. Denoted in Fig. 2(c), both components R_1 and R_1' can be coupled into R_2 and R_2', respectively, which means that part of energy in one emitter can be injected into the other one in the coupling region. The wavevectors of these four components should satisfy the following phase matching conditions: $\boldsymbol{k}_{R_1} + \boldsymbol{k}_{G_1} = \boldsymbol{k}_{R_2'}$, $\boldsymbol{k}_{R_1} + \boldsymbol{k}_{G_2} = \boldsymbol{k}_{R_2}$, $\boldsymbol{k}_{R_1'} + \boldsymbol{k}_{G_1} = \boldsymbol{k}_{R_2'}$, $\boldsymbol{k}_{R_1'} + \boldsymbol{k}_{G_2} = \boldsymbol{k}_{R_2}$ as shown in the inset of Fig. 2(c). Furthermore, R_1 and R_1' should be in phase due to the optical gain provided in the coupling region which

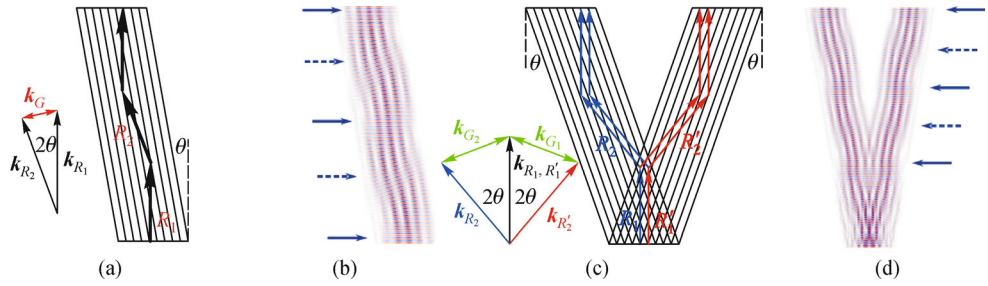

Fig. 2 Wave coupling and cavity modes in the single emitter and coupled emitter. (a) A single angled-grating emitter. R_1 and R_2 are two planewave-like components resonate with the grating. The phase matching condition between $\boldsymbol{k}$-vectors is shown in the inset; (b) FDTD simulation result of a single angled-grating resonator. The solid arrows represent the R_1 component and the dashed arrows represent the R_2 component; (c) an on-chip combined angled-grating laser. Arrows in blue represent wave components in the left grating, while arrows in red represent wave components in the right grating. The inset shows the coupling between different wavevectors through the grating; (d) FDTD simulation result of a combined angled-grating resonator

would suppress the out-phase interference. Because of the same wavevector selection mechanism in the single emitter, the wave components with the normal incident angle at two facets will be favored. FDTD simulations are carried out to show the preferred mode of a coherently combined laser cavity in Fig. 2(d). In this figure, the mode outside the coupling region is still snake-like just as same as that in a single angled-grating laser. In the coupling region, the wave components from two individual lasers constructively interfere, which means that they are efficiently coupled. Thus, mode control and coherent beam combining are simultaneously obtained through Bragg diffraction in this new laser cavity design.

The proposed approach can be expanded to a 1D coherently coupled broad-area laser array. Figure 3 shows the schematic of such a coherent array on a laser bar. Strong optical coupling of the cavity modes in the overlap region between any two adjacent lasers leads to phase locking. For each individual laser, the phase accumulated in a round-trip has to be integer multiples of 2π. Therefore, all the emitting apertures along one side of the bar are in phase. Compared to conventional coherent laser arrays, the width of each individual emitter in our design is almost two orders of magnitude larger. In addition, the Bragg diffraction based combining mechanism is much more robust against nonlinear and thermal effects. It should be pointed out that light of one emitter can be directly injected not only into the adjacent emitters through the coupling regions, but also into other emitters in the array. This implies that a large number of emitters can be coherently combined [6,35], which would lead to a bar-scale single mode diode laser with diffraction-limited output.

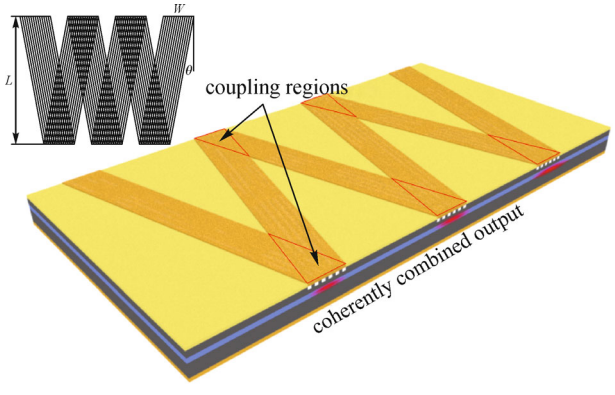

Fig. 3 Planar geometry of a zigzag coherently combined laser array. Coupling regions are marked by red triangles. Coherently combined outputs (marked in red circles) constructively interfere in the far field

3 Scalability analysis of a zigzag structure for passive coherent beam combining

In this section, we perform the scalability analysis of the proposed zigzag beam combining structure. For simplicity, a laser system with the same topographic structure is used, the schematic plot of which is shown in Fig. 4(a). The entire system consists of two groups of mirrors, two groups of couplers, and the laser emitters/gain medium at the center. The red blocks next to the left group of mirrors denote a short length of gain medium. Unlike the conventional tree-like beam combining structure [36,37] shown in Fig. 4(b), no extension of couplers along the light propagating direction is needed in the zigzag array structure when the number of emitters (N) increases, which makes the zigzag array more compact. This is an important advantage for the development of on-chip semiconductor laser systems. In general, the longer the coupler array, the more nonlinear effects and unwanted feedback it may produce, which will degrade the performance of beam combining. In addition, this proposed zigzag design will save the wafer space and increase the yield. Unlike the Y-junction laser array [38,39] in which the 2X1 coupler divides the power equally, the proposed zigzag laser array benefits more design flexibility from the 2X2 coupler since we can adjust the power

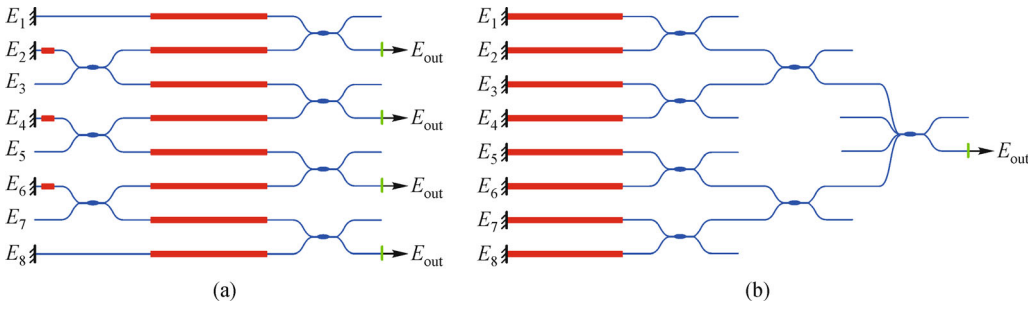

Fig. 4 Topographic structures of different passive beam combining systems. Adjacent laser beams are connected by 2X2 coupler. (a) Proposed zigzag-like structure. Each laser beam is directly coupled with adjacent neighbors. The system has $N/2$ output ports; (b) tree-like structure. The system has only one output port

division at two ports to compensate the difference among laser emitters/gain medium in the array. In the following section, based on the assumption that the system operates at a single super-mode, we detail our investigations of the array scalability by means of brightness in the presence of a certain level of phase noise.

We assume that the whole system operates at a single super-mode with a single wavelength. And we estimate the scalability of the proposed structure from the perspective of brightness which can be defined as

$$B = \frac{P}{A\Omega},$$

where P is the total optical power, A is the emitter area and Ω is the solid emission angle [40]. Let B_0 be the brightness of one single emitter in the array,

$$B_0 = \frac{P_0}{A_0\Omega_0}.$$

Thus, the ratio B to B_0 shows the improvement of brightness after combining,

$$\frac{B}{B_0} = \frac{P}{P_0}\frac{A_0\Omega_0}{A\Omega}.$$

Since the solid angle Ω can be expressed as follows:

$$\Omega = \frac{s}{r^2} \approx \frac{\pi r\theta_x r\theta_y}{r^2} = \pi\theta_x\theta_y,$$

where S is the area of the observation plane, r is the distance between the light source and the observation plane, θ_x is the divergence angle along the slow axis and θ_y is the divergence angle along the fast axis. For simplicity, the filling factor is assumed to be 1. Since the beam is almost diffraction limited along the fast axis (y direction), we have $\theta_{y,0} = \theta_{y,\mathrm{tot}}$, then

$$\frac{B}{B_0} = \frac{1}{N}\frac{P}{P_0}\frac{\theta_{x,0}}{\theta_{x,\mathrm{tot}}}.$$

To evaluate the above equation, we must calculate the far field to obtain the divergence angle, using the method in Ref. [41]. Assuming that the near field distribution of one single emitter in the array, denoted by $u_0(x)$ is Gaussian shape and identical, the near field of the array can be expressed as

$$u(x) = u_0(x) \otimes \sum_{j=1}^{N} \delta(x - jd)e^{\mathrm{i}\phi_j} = u_0(x) \otimes g(x),$$

where $\otimes$ is the convolution operator, d and ϕ_j is the random phase of each emitter. Then the far field of $u(x)$, denoted by $U(x)$ with the parameter $s_x \overset{\mathrm{def}}{=} \frac{\theta_x}{\lambda}$, is found by taking the Fourier transformation of $u(x)$. That is

$$U(s_x) = U_0(s_x)\sum_{j=1}^{N} \mathrm{e}^{(2\pi\mathrm{i}js_x d + \mathrm{i}\phi_j)} = U_0(s_x)G(s_x).$$

Then the far-field intensity can be calculated by

$$I(s_x) = \langle |U(s_x)|^2 \rangle = |U_0(s_x)|^2 \langle |G(s_x)|^2 \rangle = I_0 I_G,$$

where $\langle\ \rangle$ is the expectation operator and I_G can be expressed as follows:

$$I_G = \sum_{j=1}^{N}\sum_{l=1}^{N} \mathrm{e}^{2\pi\mathrm{i}s_x d(j-l)} \langle \mathrm{e}^{\mathrm{i}(\phi_j - \phi_l)} \rangle.$$

Thus all the phase information is included in I_G.

In the zigzag array structure, each emitter is directly coupled with the several emitters nearby. Here, we will only investigate two cases: the fully-correlated case and the adjacent-correlated case. In the fully-correlated case, the phase difference between any two elements obeys the same zero-mean Gaussian distribution. And in the adjacent-correlated case, we only require that the phase difference between the adjacent elements obeys the same zero-mean Gaussian distribution. The strength of the phase variation will be denoted by the standard deviation of the Gaussian distribution, σ_ϕ. For purposes of comparison, the ideal exemplar with no phase noise is also calculated and studied. We have to emphasize that the fully-correlated case discussed in this paper is not attainable. While it is possible to ensure a relationship among all the elements, they are not guaranteed to obey an identical distribution. Therefore, this fully-correlated case is only a simplified

and theoretical simulacrum with which we may establish the limitation of scalability.

For the ideal case,

$$I_G^{\text{ideal}} = \frac{\sin^2(\pi N s_x d)}{\sin^2(\pi s_x d)}, \tag{1}$$

and for the fully correlated case,

$$I_G^{\text{ful\_corr}} = \mathrm{e}^{\left(-\frac{\delta_\phi^2}{2}\right)} I_G^{\text{ideal}} + N\left(1-\mathrm{e}^{\left(-\frac{\delta_\phi^2}{2}\right)}\right), \tag{2}$$

and for the adjacent correlated case,

$$\begin{aligned} I_G^{\text{adj\_corr}} = {} & \frac{1}{[1-2\alpha\cos\beta+\alpha^2]^2}\Big(4\alpha^2 + N(1-\alpha^4) \\ & + 2\alpha\cos\beta[\alpha^2(N-1)-N-1] \\ & + 2\alpha^{N+1}\{\alpha^2\cos[(N-1)\beta] \\ & - 2\alpha\cos(N\beta) + \cos[(N+1)\beta]\}\Big), \end{aligned} \tag{3}$$

where $\alpha = \mathrm{e}^{-\frac{\delta_\phi^2}{2}}$ and $\beta = 2\pi s_x d$. Equations (1), (2) and (3) can be found in Ref. [41] in details.

Figure 5 shows the plots of I_G^{ideal}, $I_G^{\text{ful\_corr}}$ and $I_G^{\text{adj\_corr}}$ when $\sigma_\phi = \pi/5$. Here, the phase noise exhibits a different impact on the far-field pattern: in the fully correlated occurrence, only the amplitude decreases due to the phase noise, compared with the ideal occurrence. In the adjacent correlated case, the amplitude is decreased and the width of the main lobe is also widened. Both effects will degrade the brightness.

The results of B/B_0 with respect to σ_ϕ and with respect to N are shown in Fig. 6(a) and 6(b), respectively. Figure 6(a) shows the decrease of brightness in both fully correlated case and adjacent correlated case as σ_ϕ increases. The fully correlated case exhibits a superior performance against the phase noise than the adjacent correlated counterpart. In Fig. 6(b), the fully correlated exemplar exhibits a closely similar result as the ideal case. The only difference is a smaller slope due to the availability of less power (as shown in Fig. 5). Unlike the ideal case and fully correlated case, the adjacent correlated case exhibits a saturation behavior in brightness. When the number of elements, N exceeds a certain value, the brightness is nearly identical, allowing us to define a characteristic number by the saturation value of brightness. This number can also be regarded as the maximum number of elements that can be coherently combined. In the case shown in Fig. 6(b), the maximum number of elements is approximately 30.

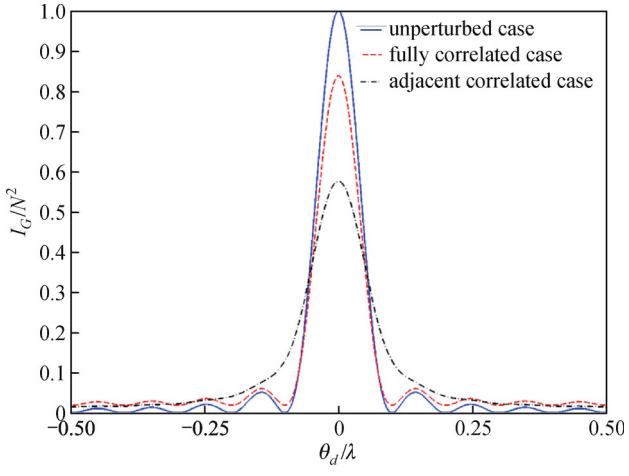

Fig. 5 Normalized I_G vs. θ_d/λ. The solid line shows the ideal case. The dash line shows the fully correlated case. The dot-dash line shows the adjacent correlated case. In the simulation, σ_ϕ is set to be $\pi/5$ [41]

The proposed zigzag array structure should be considered as a situation between the fully correlated case and the adjacent correlated case because of the coupling mechanism explained above. Consequently, the performance of our structure should be superior to the adjacent correlated case and the scalability will be larger than the characteristic number in the adjacent correlated case. Since the evanescent-wave coupled array is more like the adjacent correlated case, our laser structure should provide better performance. Compared with the coupling mechanism of the strong spatial filtering in an external common cavity (Talbot cavity [21], self-Fourier cavity [23], etc.), however, it is difficult to determine the advantage of our design. Specifically, although arrays with a common cavity are more analogous to the fully correlated simulacrum, the coupling strengths between any two emitters are not likely to be equal. Consequently, the common cavity is more likely to be in the same category as our laser structure, between the fully correlated case and the adjacent correlated case. We finally wish to emphasize that the brightness saturation is due to the locally phase-correlated emitters based upon our adjacent correlated assumption. Thus, it is reasonable to consider that as long as the locally phase-correlated assumption (not necessarily the adjacent correlated assumption) holds, brightness saturation behavior will occur.

4 Fabrications

We fabricate the proposed laser structure with two and six angled-grating broad-area lasers coherently combined in a multiple quantum well InGaAsP wafer as shown in Table 1. The fabrication process consists of a series of steps of lithography, etching, planarization and metallization. First, a SiO_2 layer is deposited by plasma enhanced chemical vapor deposition (PECVD) as a hard mask. Then

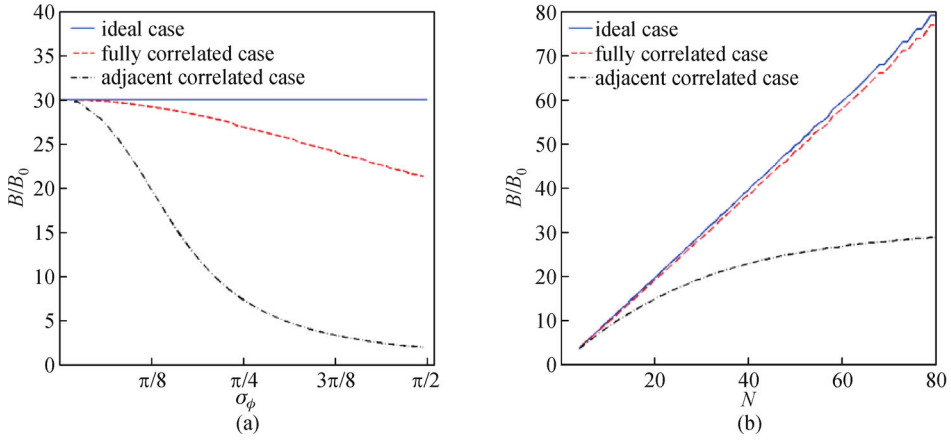

Fig. 6 (a) Brightness with respect to the standard variation of phase noise σ_ϕ. N is set to be 30 in the calculation; (b) brightness with respect to the number of emitters N. σ_ϕ is set to be $\pi/8$ in the calculation. The solid line shows the ideal case. The dash line shows the fully correlated case and the dot-dash line shows the adjacent correlated case

Table 1 $In_{1-x}Ga_xAs_yP_{1-y}$/InP epitaxy wafer design

description	material	thickness/nm	doping	x	y
substrate	InP	n/a	$n = 2e^{18}$	n/a	n/a
buffer	InP	1000	$n > 1e^{18}$	n/a	n/a
waveguide	InGaAsP	130	$n = 1e^{17}$	0.1449	0.3167
waveguide	InGaAsP	40	undoped	0.1449	0.3167
waveguide	InGaAsP	50	undoped	0.2467	0.5353
QW×4	InGaAsP	8.5	undoped	0.4402	0.9425
barrier×3	InGaAsP	10	undoped	0.2467	0.5353
waveguide	InGaAsP	50	undoped	0.2467	0.5353
waveguide	InGaAsP	40	undoped	0.2144	0.4663
waveguide	InGaAsP	120	$p = 1e^{17}$	0.2144	0.4663
cladding	InP	1000	$p = 1e^{17} - 2e^{18}$	n/a	n/a
contact layer	$In_{0.53}Ga_{0.47}As$	20	$p > 1e^{19}$	n/a	n/a

the grating structure is defined by ebeam lithography. After two steps of dry etching, the gratings are transferred into the epiwafer. Next, the structure is planarized by spinning a layer of BCB (CYCLOTENE 3022-46, bisbenzocyclobutene), and then it is etched back until the epiwafer surface exposes. After a SiO_2 insulation layer is deposited and a contact window is opened, the p-side metal contact is deposited. With the p-side metal contact protected by a thick layer of photoresist, the chip is ion implanted by H^+ to confine the injected current within the grating area. Then the whole chip is thinned and n-side metal contact is deposited. After the chip is cleaved to the desired length, the laser diode is mounted and wired on a c-mount for measurement. Figure 7 shows the scanning electron microscope (SEM) pictures of the gratings and the packaged laser diodes.

5 Results and discussion

We take measurements of *L-I* curve, optical spectrum, near field and far field of the two and six combined lasers. All the results are obtained in continuous wave (CW) operation at low temperature around 230 K, unless stated otherwise. Figures 8(a) and 8(b) show the *L-I* curve and optical spectrum of the two coherently combined laser. The threshold is around 300 mA and the slope efficiency is about 0.48 W/A. The *L-I* curve of p-side-down bonded single angled-grating broad-area laser is also shown in Fig. 8(a). Both the single and two combined lasers can go over 1 W output power at high current without thermal rollover. The dashed line represents the twice output power of a single emitter at doubled pump current ($2L_{\text{single}}$ vs. $2I_{\text{single}}$). Along all the pump currents, the *L-I*

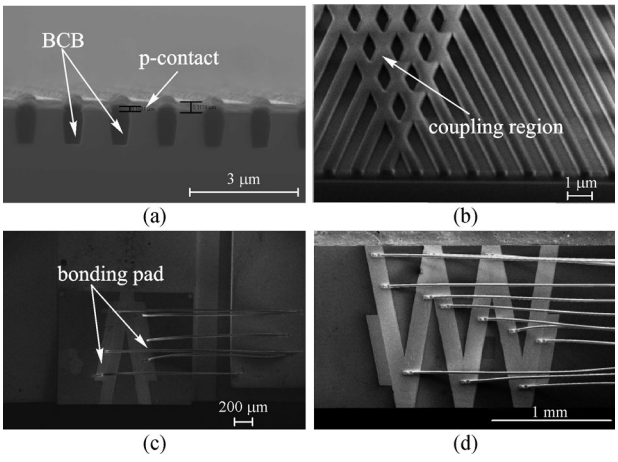

Fig. 7 SEM pictures of (a) etched gratings, (b) coupling region, (c) packaged two combined laser and (d) packaged six combined laser mini bar

curve of the combined laser (in red line) is very close to the dashed line, indicating almost 100% combining efficiency.

Figures 8(c) and 8(d) show the near field and far field measurement results of the two combined laser. In the near field shown in Fig. 8(c), the total width of the emitting aperture is about 160 μm and the distance between the two apertures is about 425.6 μm. There is about 10% difference in the intensities of the two beams. These values will be used in the theoretical far-field calculation. The near-field profile after ion implantation has sharp edges of the emitting apertures and large distinction ratio between the emitting area and dummy area due to better current confinement. In the far field shown in Fig. 8(d), an overall single lobe envelope is obtained. Multiple fringes in the far field are due to the interference of two coherently combined emitters. The full width at half maximum (FWHM) is about 1.08°. The angular distance between fringes is about 0.2073°. High contrast ratio of the interference fringes is obtained. The intensity difference between peak and valley is about 0.9 in the normalized scale. We also calculate the far-field pattern by applying Fourier transform on the measured near-field profile and compare the calculated result (green dashed line) with the measured far field (blue solid line) in Fig. 8(d). The angular distance between fringes in the calculated result is about 0.2040°. We obtain a good agreement between the two

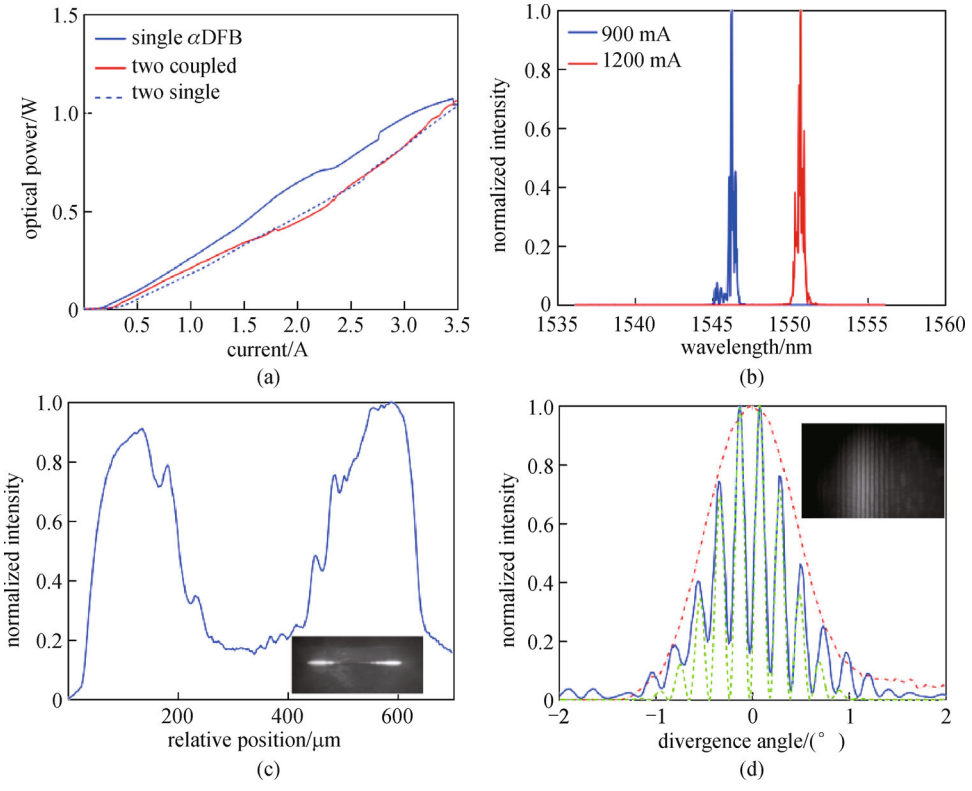

Fig. 8 (a) *L-I* curves of the p-side-down bonded single angled-grating broad-area laser (in solid blue line) and two coherently combined lasers (in red line). The dashed line is the twice of the single emitter output power at doubled pump current to be compared to the combined output; (b) spectra at two different pump currents; (c) near field of the coupled laser. The inset is the camera image; (d) far field profiles: the blue solid line is the measured far field of the coupled laser, the green dashed line is the calculated far field and the red dash-dot line represents the measured far field of a single angled-grating broad-area laser. We obtain a good agreement between the measured and calculated far field. The inset is the camera image

results. Besides, we also show the measured far field of an ion-implanted single angled-grating broad-area laser. It is presented as the red dash-dot line in the same figure. We compare the far field profile of the combined laser with that of a single emitter. If two coupled emitters are coherently combined and in-phase, they will constructively interfere in the far field and the overall envelope of the interfered far field remains the same as that of a single emitter. The only difference is that within the overall envelope, interference patterns present. This is the exact case in our measurement results. The far field envelope of two combined laser matches very well with that of a single emitter. The fine interference fringes within the far field profile of a single emitter indicate that the two angled-grating broad-area lasers are indeed coherently combined with near-diffraction-limited beam quality.

For the six combined lasers on a mini bar, Fig. 9(a) shows the light power vs. current curve. The threshold current is about 1213.6 mA. The slope efficiency is 0.362 W/A near threshold and changes to 0.247 W/A at around 2000 mA. The slope efficiency in CW operation drops mainly due to thermal effects since the slope efficiency does not drop in the quasi-CW (QCW) operation. In our mini laser bar, the optical spectra of each emitting aperture are measured through the configuration shown in Fig. 9(c). The laser bar output facet is first imaged through the obj. lenses 1. An iris is placed at the image plane after the obj. lenses 1 as a spatial filter, which lets the light from one aperture pass through and blocks the light from other apertures. This setup ensures that only the light emitting from one aperture can be collimated by the obj. lenses 2 and then collected by the collimator. At last, the collected light is characterized by an optical spectrum analyzer (OSA) through a multi-mode fiber. The optical spectra of the three emitting apertures are shown in Fig. 9(b). The three apertures have the same lasing wavelengths around 1525.3 nm with a span of 0.4 nm as shown in the inset of Fig. 9(b), which indicates good spectral coherence of the mini laser bar.

The fabricated mini laser bar has two output facets (see Fig. 3). One contains three apertures and each of them consists of the combination of two emitters. At the other side, the two middle apertures consist of the combined outputs and the other two aside only consist of the output of one emitter. Figure 10(a) shows the near field profile measured at the three-aperture facet. In this figure, the distances between the neighboring apertures are very close to each other and match well with the design parameters. The similar intensities and widths of the three apertures indicate a uniform distribution of injected current. These values are denoted in this figure and used to calculate the theoretical far field profiles. In Fig. 10(b), we show the measured and calculated far field profiles, along with the far field profile of a single angled-grating broad-area laser. High contrast ratio interference fringes are clearly observed in this figure. The measured average angular distance between fringes is about 0.2093° which is very close to the theoretical result of 0.2077°. The measured FWHM of the far field is about 1.5° which is slightly larger than the calculated result of 1.1°. All the results above demonstrate that the mini laser bar is coherently combined with near diffraction-limited beam quality. Figure 11 shows the near field and far field measurement results of the four-aperture side, respectively. In the near field profile, the two side apertures have slightly smaller intensities than the two middle apertures. Interference fringes are clearly observed in the far field profile as well, indicating good spatial coherence of this emitting facet.

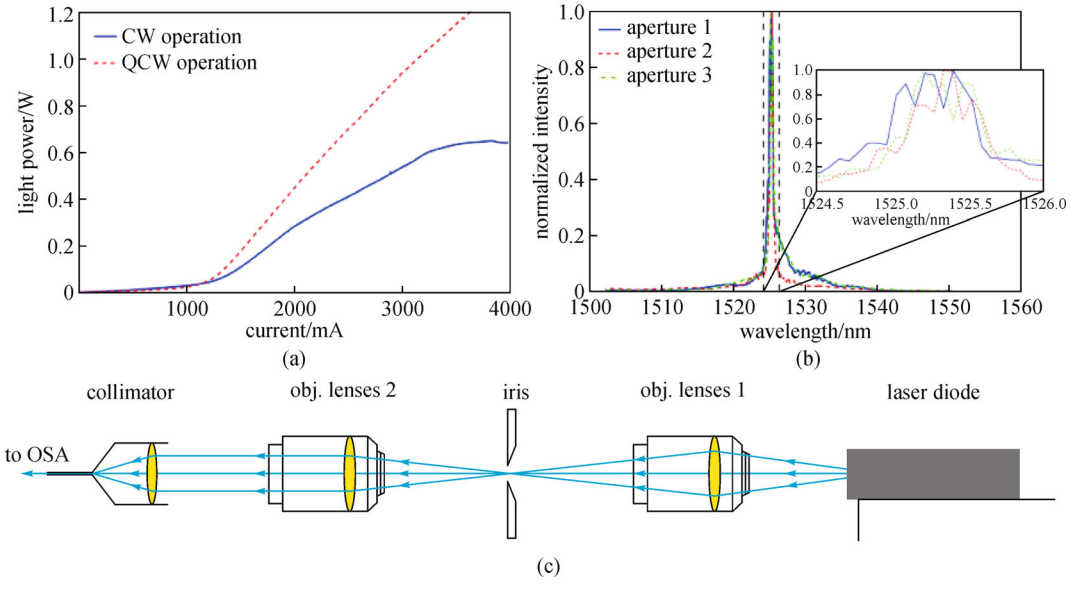

Fig. 9 (a) Light power vs. current curve of the mini laser bar; (b) light spectrum of three apertures at 2000 mA; the inset is the zoom-in view between 1524.5 and 1526.0 nm; (c) measurement setup used to take the optical spectrum of individual aperture

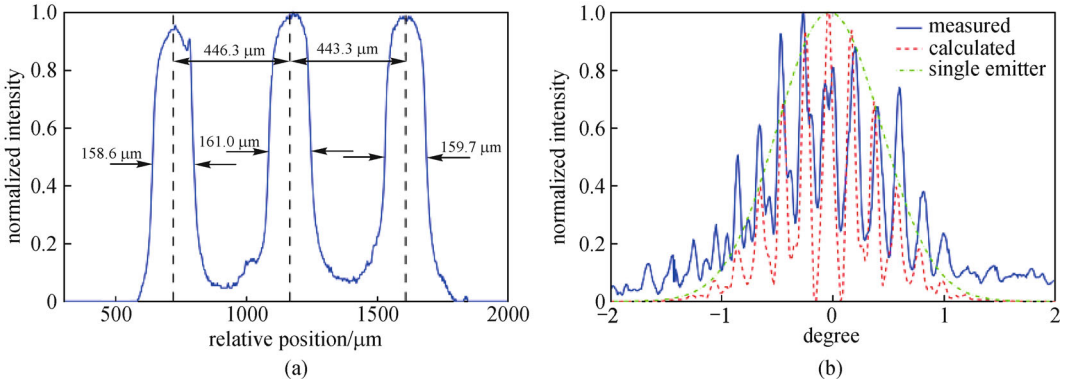

Fig. 10 Near field and far field profiles of the three coherent output apertures of a mini-bar at 2000 mA. (a) Near field profile; (b) measured far field profile (blue solid line); calculated far field profile (red dashed line); far field profile of a single angled-grating broad-area laser (green dash-dotted line)

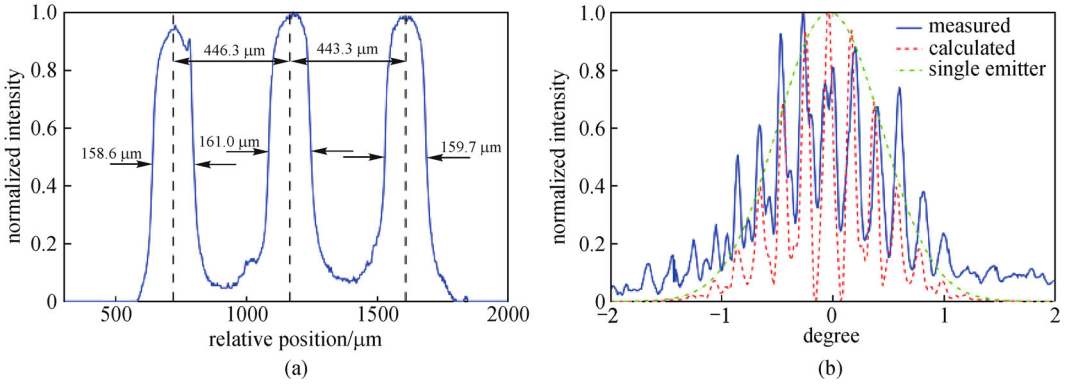

Fig. 11 Near field and far field profiles of the four coherent output apertures of a mini-bar at 2000 mA. (a) Near field profile; (b) measured far field profile

6 Conclusions

In summary, we have proposed the integrated coherent beam combining of angled-grating broad-area lasers. The scalability of the proposed zigzag-like laser array is analyzed and compared with other coherent combining methods. We have also demonstrated two and six angled-grating broad-area lasers that are coherently combined by use of the proposed method. Simultaneous modal control and coherent combining are achieved through Bragg diffraction. The far field with interference fringes in a single lobe envelope proves that the emitters in the array are indeed coherently combined with near diffraction-limited beam quality. For the two combined laser, we obtain the coherently combined output power > 1 W using p-side-down bonding. And it is shown that the combining efficiency is almost one. For the six combined laser mini bar, we also obtain over 1W output power in the QCW operation. The thermal effect is still the main reason that limits the output power at high injected current levels.

Acknowledgements The authors acknowledge funding support from Army Research Office (ARO). The authors also acknowledge the use of the Gatech Nanotechnology Research Center Facility in the completion of this work.

References

1. Hanke C. High power semiconductor laser diodes. Informacije Midem-Journal of Microelectronics Electronic Components and Materials, 2001, 31(4): 232–236
2. Ziegler M, Tomm J W, Zeimer U, Elsaesser T. Imaging catastrophic optical mirror damage in high-power diode lasers. Journal of Electronic Materials, 2010, 39(6): 709–714
3. DeMars S D, Dzurko K M, Lang R J, Welch D F, Scrifres D R, Hardy A. Angled-grating distributed feedback laser with 1 W CW single-mode diffraction-limited output at 980 nm. In: Proceedings of Summaries of papers presented at the Conference on Lasers and Electro-Optics, 1996. 1996, 77–78
4. DWong V V, DeMars S D, Schoenfelder A, Lang R J. Angled-grating distributed-feedback laser with 1.2 W CW single-mode diffraction-limited output at 10.6 μm. In: Proceedings of Summaries of papers presented at the Conference on Laser and Electro-Optics, 1998. 1998, 34–35

5. Paschke K, Bogatov A, Bugge F, Drakin A E, Fricke J, Guther R, Stratonnikov A A, Wenzel H, Erbert G, Trankle G. Properties of ion-implanted high-power angled-grating distributed-feedback lasers. IEEE Journal of Selected Topics in Quantum Electronics, 2003, 9 (5): 1172–1178
6. Fan T Y. Laser beam combining for high-power, high-radiance sources. IEEE Journal of Selected Topics in Quantum Electronics, 2005, 11(3): 567–577
7. Wirth C, Schmidt O, Tsybin I, Schreiber T, Eberhardt R, Limpert J, Tünnermann A, Ludewigt K, Gowin M, ten Have E, Jung M. High average power spectral beam combining of four fiber amplifiers to 8.2 kW. Optics Letters, 2011, 36(16): 3118–3120
8. Andrusyak O, Smirnov V, Venus G, Glebov L. Beam combining of lasers with high spectral density using volume Bragg gratings. Optics Communications, 2009, 282(13): 2560–2563
9. Chann B, Huang R K, Missaggia L J, Harris C T, Liau Z L, Goyal A K, Donnelly J P, Fan T Y, Sanchez-Rubio A, Turner G W. Near-diffraction-limited diode laser arrays by wavelength beam combining. Optics Letters, 2005, 30(16): 2104–2106
10. Vijayakumar D, Jensen O B, Ostendorf R, Westphalen T, Thestrup B. Spectral beam combining of a 980 nm tapered diode laser bar. Optics Express, 2010, 18(2): 893–898
11. Welch D F, Scifres D, Cross P, Kung H, Streifer W, Burnham R D, Yaeli J. High-power (575 mW) single-lobed emission from a phased-array laser. Electronics Letters, 1985, 21(14): 603–605
12. Kapon E, Katz J, Yariv A. Supermode analysis of phase-locked arrays of semiconductor lasers. Optics Letters, 1984, 9(4): 125–127
13. Welch D F, Cross P S, Scifres D R, Streifer W, Burnham R D. High-power (CW) in-phase locked “Y” coupled laser arrays.. Applied Physics Letters, 1986, 49(24): 1632–1634
14. Botez D, Hayashida P, Mawst L J, Roth T J. Diffraction-limited-beam, high-power operation from X-junction coupled phase-locked arrays of AlGaAs/GaAs diode lasers. Applied Physics Letters, 1988, 53(15): 1366–1368
15. Hermansson B, Yevick D. Analysis of Y-junction and coupled laser arrays. Applied Optics, 1989, 28(1): 66–73
16. Botez D, Mawst L J, Peterson G, Roth T J. Resonant optical transmission and coupling in phase-locked diode laser arrays of antiguides: the resonant optical waveguide array. Applied Physics Letters, 1989, 54(22): 2183–2185
17. Zmudzinski C, Botez D, Mawst L J, Tu C, Frantz L. Coherent 1 W continuous wave operation of large-aperture resonant arrays of antiguided diode lasers. Applied Physics Letters, 1993, 62(23): 2914–2916
18. Chang-Hasnain C, Welch D F, Scifres D R, Whinnery J R, Dienes A, Burnham R D. Diffraction-limited emission from a diode laser array in an apertured graded-index lens external cavity. Applied Physics Letters, 1986, 49(11): 614–616
19. Henderson G A, Begley D L. Injection-locked semiconductor laser array using a graded-index rod: a computational model. Applied Optics, 1989, 28(21): 4548–4551
20. Waarts R, Mehuys D, Nam D, Welch D, Streifer W, Scifres D. High-power, CW, diffraction-limited, GaAlAs laser diode array in an external Talbot cavity. Applied Physics Letters, 1991, 58(23): 2586–2588
21. Mehuys D, Streifer W, Waarts R G, Welch D F. Modal analysis of linear Talbot-cavity semiconductor lasers. Optics Letters, 1991, 16 (11): 823–825
22. Liu B, Liu Y, Braiman Y. Coherent beam combining of high power broad-area laser diode array with a closed-V-shape external Talbot cavity. Optics Express, 2010, 18(7): 7361–7368
23. Corcoran C J, Pasch K A. Modal analysis of a self-Fourier laser. Journal of Optics. A, Pure and Applied Optics, 2005, 7(5): L1–L7
24. Corcoran C J, Durville F. Experimental demonstration of a phase-locked laser array using a self-Fourier cavity. Applied Physics Letters, 2005, 86(20): 201118
25. Goldberg L, Weller J F, Mehuys D, Welch D F, Scifres D R. 12 W broad area semiconductor amplifier with diffraction-limited optical output. Electronics Letters, 1991, 27(11): 927–929
26. Walpole J N, Kintzer E S, Chinn S R, Wang C A, Missaggia L J. High-power strained-layer InGaAs/AlGaAs tapered traveling wave amplifier. Applied Physics Letters, 1992, 61(7): 740–742
27. Shay T M, Benham V, Baker J T, Sanchez A D, Pilkington D, Lu C A, 0. Self-synchronous and self-referenced coherent beam combination for large optical arrays. IEEE Journal of Selected Topics in Quantum Electronics, 2007, 13(3): 480–486
28. Cheung E C, Ho J G, Goodno G D, Rice R R, Rothenberg J, Thielen P, Weber M, Wickham M. Diffractive-optics-based beam combination of a phase-locked fiber laser array. Optics Letters, 2008, 33(4): 354–356
29. Goodno G D, McNaught S J, Rothenberg J E, McComb T S, Thielen P A, Wickham M G, Weber M E. Active phase and polarization locking of a 1.4 kW fiber amplifier. Optics Letters, 2010, 35(10): 1542–1544
30. Uberna R, Bratcher A, Alley T G, Sanchez A D, Flores A S, Pulford B. Coherent combination of high power fiber amplifiers in a two-dimensional re-imaging waveguide. Optics Express, 2010, 18(13): 13547–13553
31. Wickham M. Coherent beam combining of fiber amplifiers and solid-state lasers including the use of diffractive optical elements. In: Proceedings of Conference on Lasers and Electro-Optics, OSA. 2010, paper CThG2
32. Augst S J, Montoya J, Creedon K, Kansky J, Fan T Y, Sanchez-Rubio A. Intracavity coherent beam combining of 21 semiconductor gain elements using SPGD. In: Proceedings of CLEO: Lasers and Electro-Optics. 2012, paper CTu1D.1
33. Huang R K, Chan B, Missaggia L J, Augst S J, Connors M K, Turner G W, Sanchez-Rubio A, Donnelly J P, Hostetler J L, Miester C, Dorsch F. Coherently combined diode laser arrays and stacks/ In: Proceedings of CLEO: Quantum Electronics and Laser Science. 2009, paper CWF1
34. Sarangan A M, Wright M W, Marciante J R, Bossert D J. Spectral properties of angled-grating high-power semiconductor lasers. IEEE Journal of Quantum Electronics, 1999, 35(8): 1220–1230
35. Glova A F. Phase locking of optically coupled lasers. Quantum Electronics, 2003, 33(4): 283–306
36. Wu T W, Chang W Z, Galvanauskas A, Winful H G. Model for passive coherent beam combining in fiber laser arrays. Optics Express, 2009, 17(22): 19509–19518
37. Chang W Z, Wu T W, Winful H G, Galvanauskas A. Array size scalability of passively coherently phased fiber laser arrays. Optics Express, 2010, 18(9): 9634–9642

38. Chen K L, Wang S. Single-lobe symmetric coupled laser arrays. Electronics Letters, 1985, 21(8): 347–349
39. Chen K, Wang S. Analysis of symmetric Y junction laser arrays with uniform near field distribution. Electronics Letters, 1986, 22(12): 644–645
40. Bachmann F, Loosen P, Poprawe R, eds. High Power Diode Lasers. In:Ultrashort Pulse Laser Technology. Berlin: Springer, 2006
41. Nabors C D. Effects of phase errors on coherent emitter arrays. Applied Optics, 1994, 33(12): 2284–2289

Yunsong Zhao obtained the Bachelor degree in electronic engineering from Tsinghua University in 2008 and the Ph.D. in electrical engineering from Clemson University in 2015. While at Clemson University, his major work was the integrated coherent beam combining of broad-area semiconductor lasers for high power and high brightness applications using transverse Bragg resonant gratings and photonic periodic nanostructures. His current research interests include high power and high brightness integrated coherently combined diode laser arrays, optoelectronic devices and integrated photonic circuits.

Yeyu Zhu received the B.Eng. degree in electrical engineering from Chongqing University, China, in 2011. And he received the M.S. degree in optical engineering from University of Electronic Science and Technology of China, Chengdu, China, in 2014. He is currently working toward the Ph.D. degree in electrical engineering in Clemson University, Clemson, USA. His research interests include semiconductor lasers and photonic periodic nanostructures.

Lin Zhu obtained the Ph.D. degree in electrical engineering from California Institute of Technology in 2008. While at Caltech, his work mainly focused on the modal control of high power, broad area semiconductor lasers using photonic periodic nanostructures. Dr. Zhu's current research interests include high power, high beam quality diode laser arrays, beam combining, optomechanics, and plasmonic devices. His work has been funded by many federal and state agencies, including ARO, DARPA, NSF, SC Space Grant, SC EPSCoR/IDeA, and ORAU. Dr. Zhu was the recipient of the DARPA Young Faculty Award, ARO Young Investigator Award, and ORAU Ralph E. Powe Junior Faculty Enhancement Award. He has served on the technical committee of IEEE/OSA CLEO conferences.